Investigating the effect of in-plane spin directions for precessing binary black hole systems

Chinmay Kalaghatgi[1] and Mark Hannam[1,2,3]

[1]*School of Physics and Astronomy, Cardiff University, Queens Buildings, Cardiff, CF24 3AA, United Kingdom*
[2]*Dipartimento di Fisica, Università di Roma "Sapienza", Piazzale A. Moro 5, I-00185 Roma, Italy*
[3]*INFN Sezione di Roma, Piazzale A. Moro 5, I-00185 Roma, Italy*

(Received 25 August 2020; revised 3 December 2020; accepted 15 December 2020; published 12 January 2021)

In gravitational-wave observations of binary black holes (BBHs), theoretical waveform models are used to infer the black-hole properties. There are several sources of potential systematic errors in these measurements, including due to physical approximations in the models. One standard approximation is to neglect a small asymmetry between the $+m$ and $-m$ spherical-harmonic modes; this is the effect that leads to emission of linear momentum perpendicular to the orbital plane, and can result in large recoils of the final black hole. The asymmetry is determined by both the magnitude *and* direction of the spin components that lie in the orbital plane. We investigate the validity of this approximation by comparing numerical relativity (NR) simulations of single-spin NR systems with varying in-plane spin directions and magnitudes (including several "superkick" configurations). We find that the mode asymmetry will impact measurements at signal-to-noise ratios (SNRs) between 15 and 80, which is well within current observations. In particular, mode asymmetries are likely to impact measurements at comparable SNRs to those at which we might hope to make the first unambiguous measurements of orbital precession. We therefore expect that models will need to include mode-asymmetry effects to make unbiased precession measurements.

DOI: 10.1103/PhysRevD.103.024024

I. INTRODUCTION

Since the advent of the Advanced LIGO [1] and Virgo [2] gravitational-wave detectors in 2015, up to October 2019 there have been a total of 50 gravitational wave signals detected which include multiple binary-black hole mergers, binary neutron star mergers and possible neutron-star-black-hole merger [3–11]. The BBH observations have begun to reveal the astrophysical rate of black-hole mergers, and the astrophysical distribution of black-hole masses and spins [12–14]. To measure the binary's properties the detector data are compared against a set of theoretical model waveforms. The accuracy of the measured parameters depends not only on the details of the source, the signal-to-noise ratio (SNR) of the signal, and parameter degeneracies, but also on the accuracy of the waveform models. Two families of waveform models, `IMRPhenom` [15–20] and `SEOBNR` [21–25], were used to calculate the reported parameters during the first two observation runs. Both rely on several physical approximations, as discussed in, for example, Ref. [26]. In this paper we test the validity and impact of a subset of those approximations.

Binary-black-hole inspiral is the result of orbital energy and angular momentum loss through gravitational radiation. If the radiation from a binary is decomposed into spin-weighted spherical harmonics, ${}^{-2}Y_{\ell m}(\theta,\phi)$, the signal is dominated by the "quadrupole" contribution in the $\ell = 2$ harmonics. Gravitational waves also carry linear momentum, and for nonspinning or aligned-spin binaries (where the black-hole spins $\mathbf{S}_i$ are parallel to the orbital angular momentum, $\mathbf{L}$, so that $\mathbf{L} \times \mathbf{S}_i = 0$), the resultant recoil of the center-of-mass within the orbital plane is manifest in the signal through interplay between different multipoles; see, for example, Ref. [27]. Current aligned-spin binary waveform models that include higher multipoles capture all of these physical effects, with varying degrees of accuracy [16,22,28]. In generic binaries, where the spins are misaligned with the orbital angular momentum, the orbital plane and spins precess during the inspiral. Generic binaries also radiate linear momentum perpendicular to the orbital plane. This effect, which shows up in the GW signal through an asymmetry between the $+m$ and $-m$ multipoles, is not present in current precessing `SEOBNR` [29] and `IMRPhenom` [30] models. Although these models include the spin directions while computing the precession dynamics used to generate the precessing waveform, the effect of varying spin directions on the full waveforms remains unmodeled. Our goal is to make a first estimate of the effect of these omissions on GW source parameter measurements.

We begin by describing in more detail the phenomenology of BBH systems, and the construction of generic-binary waveform models.

 © 2021 American Physical Society

A BBH system undergoing non-eccentric inspiral can be characterized by eight parameters, the individual masses (m_i), and the components of the two spin vectors $(\mathbf{S}_i)$, specified at some fiducial point during the inspiral, for example a chosen orbital frequency. The GW signal is also parametrized by the binary's sky-position (α, δ), inclination (ι), coalescence phase (ϕ_c), distance (d_L), polarization (ψ) and time of arrival (t_c) at the detector. As noted above, the complex GW strain can be decomposed into spin-weighed spherical harmonics as,

$$h(t,\theta,\phi) = h_+(t) - ih_\times(t) = \sum_{\ell,m} h_{\ell m}(t)\,{}^{-2}Y_{\ell m}(\theta,\phi), \quad (1)$$

where (θ, ϕ) give the position of the observer on a sphere centered on the center-of-mass of the binary.

Based on the black-hole (BH) spin configurations, coalescing BBH systems with spins can be considered to be either:

(i) Aligned-spin: The BH spins are parallel or antiparallel to $\mathbf{L}$, so $\mathbf{L} \times \mathbf{S}_i = 0$, where $i = 1, 2$ for each BH. From the symmetries of the system, the BHs orbit in a fixed plane, i.e., the direction of the orbital angular momentum $\hat{\mathbf{L}}$ remains fixed. In the frame where $\hat{\mathbf{L}} \| \hat{z}$, symmetry also implies that

$$h_{\ell,m} = (-1)^\ell h^*_{\ell,-m}, \quad (2)$$

and that any linear momentum emission is perpendicular to $\mathbf{L}$; although the orientation of the orbital plane remains fixed, the center-of-mass can recoil within this plane.

(ii) Precessing: One or both BHs have nonzero spin components perpendicular to $\hat{\mathbf{L}}$. We denote the parallel components by $\mathbf{S}_i^{\|}$ and the perpendicular components by $\mathbf{S}_i^{\perp}$. The presence of $\mathbf{S}_i^{\perp}$ causes the orbital plane to precess over the course of the coalescence. This leads to modulations of the amplitude and phase of the waveform. Emission of linear momentum is now also possible perpendicular to the orbital plane, which breaks the symmetry of Eq. (2) between the $\pm m$ multipoles.

As was shown in previous studies [31–33], a precessing waveform can be decomposed into the waveform as observed in a co-precessing frame, h^{CP}, and a time- or frequency-dependent rotation that describes the precessional dynamics. The rotation can be expressed in terms of three Euler angles, (α, β, γ), and the $\ell = 2$ modes of the precessing-binary waveform h^{P} constructed as

$$h^{\mathrm{P}}_{2m} = e^{im\alpha} \sum_{m'} e^{-im'\epsilon} d^2_{mm'}(\beta) h^{CP}_{2m'}, \quad (3)$$

where $d^2_{mm'}$ denote the $\ell = 2$ Wigner-d matrices. In the current precessing models (`IMRPhenom` and `SEOBNR`), the coprecessing-frame waveform is based on an underlying nonprecessing-binary model (with some modifications), and this procedure preserves its orbital-plane symmetry, Eq. (2). These models therefore do not include the $\pm m$ mode asymmetry of full precessing-binary waveforms.

The magnitude and direction of the out-of-plane angular momentum loss $\dot{p}_{\|}$ (and therefore the level of mode asymmetry) is related to the angles between the in-plane spins $\mathbf{S}_i^{\perp}$ and the separation vector between the two black holes $\hat{\mathbf{n}}$, as most easily seen in the PN treatment in Sec. III. E of Ref. [34]. During one orbit the spin directions change little, so $\dot{p}_{\|}$ oscillates approximately on the orbital timescale. In the "twisted-up" models described above, this effect is not present, and an overall rotation of the spin(s) in the orbital plane introduces only an offset in the precession angle α, which is degenerate with the azimuthal angle, ϕ, since it enters the spin-weighted spherical harmonics as $e^{im\phi}$. The model waveforms are therefore degenerate with respect to a constant rotation of the in-plane spins, while true waveforms include an additional effect that varies sinusoidally with respect to this spin rotation.

Out of plane recoil in the context of mode asymmetries has been discussed in NR simulations in [35], and further illustration of the effect in GW signals is shown in [26]. Earlier studies on in-plane effects on waveforms and/or mode-asymmetries for precessing systems include [36–38].

In this study, we investigate the effects of varying the in-plane spin direction for single-spin precessing NR waveforms for a given combination of mass-ratio and spin. We also consider the special case of the "super-kick" configuration [35,39,40]: these are equal-spin configurations where the spins lie entirely in the orbital plane, and $\mathbf{S}_1 = -\mathbf{S}_2$. Due to the symmetry of this configuration, the orbital plane does not precess, but *does* bob up and down due to linear momentum loss, making this an especially clean system for the study of mode asymmetry. We choose these configurations to estimate the importance of mode-asymmetric content on parameter measurements. Using the waveform with in-plane spin initially aligned to the position vector as a *proxy template*, we compute matches (see Sec. III A) against systems with different in-plane spin directions. Using a relationship between the match value and SNR at which two signals are distinguishable, we provide an estimate of the SNR at which mode asymmetries will impact parameter measurements. We also use a selection of waveforms with the same spin direction as the proxy template but with differing in-plane spin magnitude to estimate the relative strength of the effect of varying spin direction versus varying spin magnitude.

For all results, we use only the $(\ell = 2, m = \pm 2)$ modes of the waveforms in the coprecessing frame. Higher modes are much weaker than the $(\ell = 2, |m| = 2)$ multipoles, but far stronger than the asymmetry contribution to the dominant modes, and we choose to consider only the dominant

modes in order to more easily isolate effects due to the mode asymmetry.

The paper is organized as follows. Section II provides details of the simulations generated for this study, Sec. III A and Sec. III B discuss the computation of precessing matches and the connection between the match and detectable SNR respectively. The specific results presented are motivated in Sec. IV with the actual results in Sec. V. The conclusions we draw from this work, and some of its limitations and potential future extensions, are discussed in Sec. VI.

II. NR WAVEFORMS

For this study, a set of 12 new NR simulations were performed with the BAM code [41,42]. Configurations are defined by the mass ratio, $q = m_2/m_1$, where we choose the convention $m_2 > m_1$, and the spin vectors specified at the start of the simulation, $\mathbf{S}_i$. In the unequal-mass simulations, only the larger black hole is spinning, so that $\mathbf{S}_1 = 0$. (We could also assign spin to the secondary black hole, but placing spin on one black hole is sufficient to produce the asymmetry effects that we wish to study.) For these simulations we can completely specify the spin direction at the beginning of the simulation by two angles, (i) the angle between the spin vector and angular momentum vector, which we call θ_{SL}, and (ii) the angle between the separation vector ($\vec{n}$) and the projection of spin onto the orbital plane ($\mathbf{S}_i^{\perp}$), which we call $\phi_{\rm Sn}$. The codes available at the beginning of this study for initial data generation did not allow for user specified $(\theta_{SL}, \phi_{\rm Sn})$ values, and so an iterative method was developed for obtaining the required initial parameters for single-spin precessing systems. The initial data generation method is described in detail Appendix. Section II A gives the details of the simulations with parameters of all the simulation listed in Table I.

A. Details of the simulations

The simulations are split into three sets based on the mass-ratio of the system: $q = 2$, $q = 4$ and a super-kick series at $q = 1$.

The $q = 2$ series is a set of four $q = 2$ NR waveforms with a total in-plane spin of (dimensionless) magnitude $\chi_2 = S_2/m_2^2 = 0.7$, with $\theta_{SL} = \pi/2$ and $\phi_{\rm Sn} = (0, \pi/2, \pi, 3\pi/2)$. For the $q = 4$ series, the spin is $\chi_2 = 0.8$, with the same $(\theta_{SL}, \phi_{\rm Sn})$ configurations as for the $q = 2$ series.

The $q = 1$ simulations are two-spin systems in the "super-kick" configuration, where both black holes are spinning, with equal and opposite in-plane spins of $\chi_i = 0.8$. The super-kick configurations are nonprecessing and due to the symmetry of the system, the final recoil is along $\pm\hat{z}$.

For the simulation names, the following convention is used: q(mass-ratio of system)a(total spin of system)× p(value of $\phi_{\rm Sn}$), following which, the first simulation in the $q = 2$ series is q2a07p0. The angle, θ_{SL}, between $\hat{L}$ and $\hat{S}$ is always $\pi/2$ for these systems, i.e., $\mathbf{S}_i^{\parallel} = 0$. For the $q = 1$ series waveforms, remember that the total spin satisfies $\mathbf{S}_1 + \mathbf{S}_2 = 0$, but we follow the above naming convention with "sk" in subscript for simplicity. We also use three extra NR simulations with different total in-plane spin magnitudes (with same θ_{SL} and $\phi_{\rm Sn} = 0$), which are used as comparison cases, and were produced as part of the waveform catalogue presented in Ref. [43].

For the $q = 2$ series, once the parameters for the $\phi_{\rm Sn} = 0$ configuration were obtained, the parameters for the other simulations in the series were obtained simply by rotating the initial spin in the plane; the resulting eccentricities were all within our tolerance. For the $q = 4$ and $q = 1$ series, however, the initial-parameter code was run separately for each value of $\phi_{\rm Sn}$.

Initial momenta consistent with low-eccentricity inspiral were estimated using the PN/EOB evolution code described in Refs. [44–46], with modifications as discussed in Appendix. We perform a short simulation of less than $1000M$ duration, and estimate the eccentricity from the coordinate separation, as given in Eq. (3) of Ref. [47]. For the $q = 2$ and $q = 1$ series, the eccentricities were all $<5 \times 10^{-3}$, and we used the same initial momenta for production simulations. For the $q = 4$ configurations, however, further eccentricity reduction was required.

Reference [45] describes an efficient procedure to further reduce eccentricity for nonprecessing binaries. For the precessing simulations used here, we adopted a simpler procedure: we performed a series of simulations with momenta increased or decreased by multiples of 0.1%, until an eccentricity below our threshold was obtained. Note that the eccentricity for a system with $\phi_{\rm Sn} \to \phi_{\rm Sn} \pm \pi$ has the same value.

BAM's mesh-refinement scheme is constructed as described in Refs. [41,42]. In particular, a nested set of boxes centred on each black hole. For each simulation in this series, the boxes around the BHs consisted of 80 points in each direction, with a grid-spacing on the finest level of $m_1/56$, $m_1/36$ and $m_1/44$ for the $q = 1$, $q = 2$ and $q = 4$ series respectively. Further details of the grid setups are provided in Ref. [43]. For two of the cases (q2a07p0 and q2a07p90), we performed higher-resolution runs with 96-point boxes, and a finest-level resolution of $m_1/48$. Using these two waveforms, we computed the match between the different resolution runs over a range of (θ, ϕ) values [see Eq. (1)] using only the $l = 2$ modes (as these are the modes used throughout the paper). We find that over the range of (θ, ϕ) values considered, we obtain matches of ∼0.9995–0.99995. This shows that using the 96 point runs will not qualitatively change our results, but we will discuss this in more detail in Sec. IV; see discussion pertaining to Fig. 1.

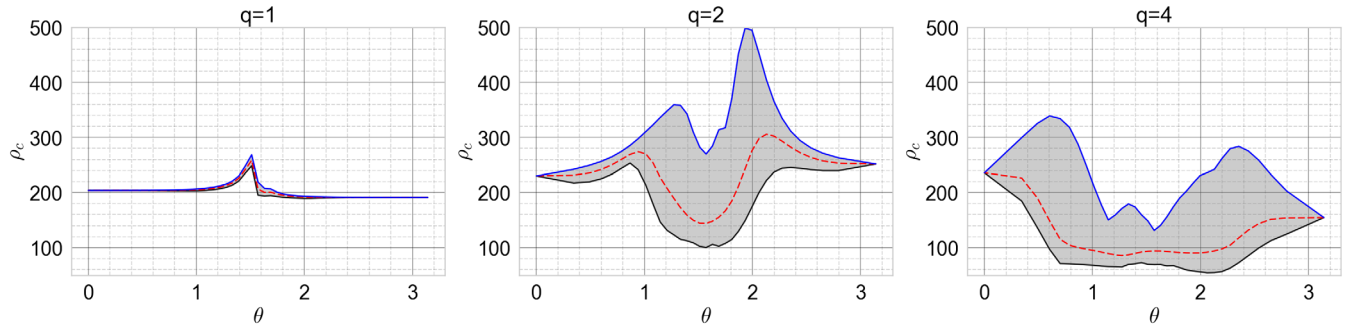

FIG. 1. The left, middle, and right columns show ρ_c for signals q1a08p180$_{sk}$, q2a07p180, and q4a08p180 as seen by templates q1a08p0$_{sk}$, q2a07p0, and q4a08p0 respectively, across the signal θ space. For each signal θ, the match is computed with the template at $\theta + \pi$, over a range of ϕ values, and the black, dashed-red and blue lines show the minimum, mean and maximum match (ρ_c) across the ϕ space. We observe a larger variation of ρ_c for the $q = 2$ and $q = 4$ cases as compared to the $q = 1$ due to presence of nonzero subdominant modes, $(l, m) = (2, 1)$, (2,0) and (2,-1).

III. ANALYSIS METHODS

This section provides the details of the match computation procedure employed for computing matches between the various precessing waveforms and the connection between the match and the SNR at which the template and signal can be distinguished from each other. This is the primary method we use to interpret the results in Sec. V.

A. Match computations

For the given physical system (with fixed intrinsic parameters), the detector response is uniquely determined by the system's sky-position, inclination (ι), coalescence-phase (ϕ_c), polarization (ψ) and time of arrival (t_c). The level of agreement between two gravitational waveforms can be ascertained by computing the match, $\mathcal{M}$, between the two waveforms. A value of $\mathcal{M} = 1$ implies the waveforms are in perfect agreement. The smaller the value of $\mathcal{M}$, the larger the disagreement between the two waveforms.

For a GW source directly overhead the detector, i.e., $(\alpha, \delta) = (0, 0)$, the real valued detector response ($h_{\rm det}(t, \vec{\lambda})$), in terms of the two gravitational wave polarizations is,

$$h_{\rm det}(t, \vec{\lambda}) = h_+ \cos(2\psi) + h_\times \sin(2\psi) = \mathrm{Re}[h(t, \vec{\lambda}) e^{2i\psi}], \tag{4}$$

with h_+ and $h_\times$ as defined in Eq. (1). Here, due to $(\alpha, \delta) = (0, 0)$, the individual detector response depends only on ψ.

For precessing systems, the match between the signal ($\tilde{h}_s(f)$) and template ($\tilde{h}_t$) waveform is given by [48],

$$\max_{\sigma} \left\langle \frac{\tilde{h}_s(f)}{\|\tilde{h}_s(f)\|} \middle| \frac{\tilde{h_t}(f)}{\|\tilde{h_t}(f)\|} \right\rangle = \frac{M}{\|\tilde{h_s}(f)\|} \sqrt{\frac{N_1 - N_2 \cos(\sigma_n + 2\sigma_m)}{N_1^2 - N_2^2}}. \tag{5}$$

where,

$$N_1 = \int_{-\infty}^{\infty} \frac{|\tilde{h}_t(f)|^2}{S_n(|f|)} \mathrm{d}f, \qquad N_2 e^{i\sigma_n} = \int_{-\infty}^{\infty} \frac{\tilde{h}_t(f)\tilde{h}_t(-f)}{S_n(|f|)} \mathrm{d}f. \tag{6}$$

and

$$M e^{i\sigma_m} = \int_{-\infty}^{\infty} \frac{\tilde{h}_t^*(f)}{S_n(|f|)} [\tilde{h}_s(f) e^{2i\psi} + \tilde{h}_s^*(-f) e^{-2i\psi}]. \tag{7}$$

Given a template and signal waveform with given signal polarization, Eq. (5)-Eq. (7) give the match optimized over template polarisation. For further details on computation of match as above, see Appendix B of Ref. [48].

For the match computations in this study, the $\phi_{\rm Sn} = 0$ system from each of the $q = 1$, $q = 2$, and $q = 4$ series of NR simulations is used as the *proxy* template with the other waveforms in each corresponding series as the signal waveforms. For the match computations, the signal is recomposed from only the $\ell = 2$ modes using Eq. (1) and Eq. (4). Each signal is uniquely defined by its inclination θ^s, phase ϕ^s, and polarisation ψ^s. (Note that we are considering a single detector network with the sky-position of the system exactly overhead the detector. Hence the angles (θ, ϕ) can be interpreted as the inclination and phase with respect to the detector.) For each unique signal, the match is maximised over the template $(\theta^t, \phi^t, \psi^t)$. A total mass of 100 $M_\odot$ is used for both signals and templates, PSD used is the `aLIGOZeroDetHighPower` PSD from LALSimulation package of LALSuite and the match is computed with $(f_{\rm min}, f_{\rm max}) \in (20, 600)$ Hz.

For each system, the signals (θ^s, ϕ^s) are isotropically distributed over a sphere with 30 points in θ^s and 25 points in ϕ^s. For each signal (θ^s, ϕ^s), we choose four values of $\psi^s \in [0, \pi/2)$ and then maximise the match over the template $(\theta^t, \phi^t, \psi^t)$. The match maximisation procedure goes through the following four steps,

(i) Isotropically grid the template (θ^t, ϕ^t) space over the sphere with 41 points in θ^t and 81 points in ϕ^t.
(ii) For each value of template θ^t_i, we compute the match across template ϕ^t_j. For each (θ^t_i, ϕ^t_j) combination, the code gives the match optimized over template ψ^t.
(iii) For each θ^t_i, the match is interpolated over the ϕ^t_j values, from which the maximum match over ϕ^t for each θ^t_i is obtained.
(iv) Thus, we get a set of match values across the template θ^t_i values, which are then interpolated to obtain the maximum match over template $(\theta^t, \phi^t, \psi^t)$.

The choice of 41×81 grid for the template waveforms for match maximization was chosen by balancing the (i) accuracy of final result and (ii) computational time required for each match computation. Using a few random signal (θ, ϕ) values, we found that doubling the grid size changed the results by at most 5% while doubling the computational cost.

B. Confidence intervals from match values

Given two waveforms close to each other in the parameter space, i.e., $h_1(\vec{\lambda_1})$ and $h_2(\vec{\lambda_2})$ such that $\vec{\lambda_1} \sim \vec{\lambda_2}$, where we have the SNR (ρ) of the signals and the match $(\mathcal{M})$ between the two, both waveforms will have consistent posterior distributions within 90% confidence interval of each other if,

$$\mathcal{M}[h_1, h_2] \geq 1 - \frac{\chi^2_k(1-p)}{2\rho^2}. \tag{8}$$

Alternatively, two waveforms would be distinguishable from each other if the posteriors recovered for the two have different confidence intervals. So, given a match value, the above gives us a condition for the SNR (ρ_c) at which the waveforms would be distinguishable,

$$\rho_c \geq \sqrt{\frac{\chi^2_k(1-p)}{2(1-\mathcal{M})}}. \tag{9}$$

For the systems under consideration, there are a total of 7 parameters which can be varied and hence, $k = 7$. At $k = 7$ for 90% confidence intervals, $\chi^2_k(1-p) = 12.02$.

See Ref. [49] for a detailed discussion for the condition used above, although previous studies [50–54] have used similar definitions to determine the distinguishability/accuracy requirements of gravitational waveforms. As was pointed out in Ref. [55], the equality in Eq. (9) is a sufficient, but not always a necessary condition, to determine the accuracy between two waveforms. For a given signal and template waveform with maximum match $\mathcal{M}$ and corresponding ρ_c, if the signal $\rho < \rho_c$, biases due to detector noise will dominate biases due to model systematics. Alternatively, if the opposite is true, biases *may* arise during parameter inference and so, the above equality is a conservative estimate of accuracy requirements. Hence, using the set of match values computed from Sec. III A for each system and Eq. (9), we can then estimate the SNR (ρ_c) at which the signal system could be distinguished by the proxy template.

IV. ORGANIZATION OF RESULTS

In subsequent sections we study the SNR (ρ_c) at which configurations with differing spin directions or spin magnitudes are distinguishable, as defined by Eq. (9). In this section we make some general comments on the accuracy of ρ_c for our simulations, some general properties of the waveforms with respect to changes in the in-plane spin direction, $\phi_{\rm Sn}$, and examine how ρ_c varies with respect to different binary orientations. This motivates the way we will present our results for the remainder of this paper.

Let us first discuss accuracy. As reported in Sec. II, the matches between the 80- and 96-point runs (for q2a07p0 and q2a07p90) are ∼0.9995–0.99995, which translates to ρ_c between 110 and 350. This suggests that we can identify two waveforms as indistinguishable up to SNRs of at least 110. We also computed the matches between the $\phi_{\rm Sn} = 0$, $\pi/2$ systems using the corresponding 80- and 96-point waveforms over a range of (θ, ϕ) values, and found that the relative error between them is $\mathcal{O}(0.05\%)$. These numbers suggest that although we should be cautious when interpreting very large values of ρ_c, we expect the qualitative behavior of the matches to remain unchanged with more accurate simulations.

Given the accuracy limits of our simulations, we are now in a position to study how the waveforms vary with respect to different initial directions of the in-plane spin. We begin by noting an approximate symmetry between systems with a $\phi_{\rm Sn}$ difference of π. An in-plane spin rotation of π corresponds to flipping the direction of the out-of-plane recoil, and therefore we would expect that the signal from a system with a given value of $\phi_{\rm Sn}$ to be identical to that from a system with $\phi_{\rm Sn} + \pi$, if observed from the opposite side of the orbital plane, i.e., with $\theta \to \theta + \pi$. We have verified that the optimal match is indeed found when $\theta_{\rm template} \approx (\theta_{\rm signal} + \pi)$. In Fig. 1 we plot the ρ_c across signal θ for a range of signal ϕ for which $\mathcal{M}$ is computed with $(\theta_{\rm template}, \phi_{\rm template}) = (\theta_{\rm signal} + \pi, \phi_{\rm signal})$ and the match is optimized only over template ψ. The $\rho_c \geq 100$ for all $\phi_{\rm Sn} = \pi$ signals for the $q = 1$ and $q = 2$ systems, with the $\rho_c \geq 50$ for each $\theta_{\rm signal}$ for $q = 4$ system. We do not observe an exact symmetry (i.e., a mismatch of zero), because in the $q = 1$ and $q = 4$ systems, we did not simply rotate the spin between each configuration, but instead calculated initial parameters individually for each value of $\phi_{\rm Sn}$, so these do not form a one-parameter family. Even with rotated spins within a series, as in the $q = 2$ series, we have not changed the momenta; we would expect even lower mismatches if the out-of-plane momenta, in the

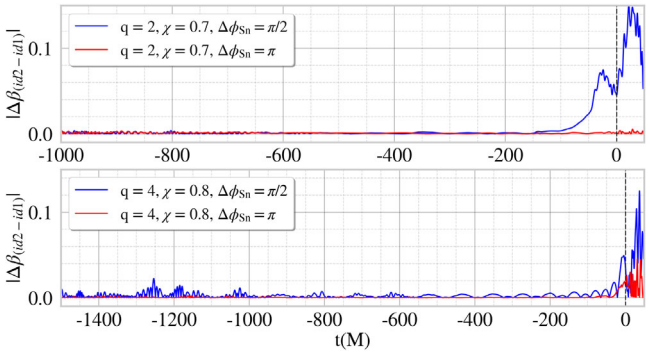

FIG. 2. Top panel: difference in the β Euler-angle (in radians) between the $\phi_{\rm Sn} = 0, \pi/2$ (Blue) and $\phi_{\rm Sn} = 0, \pi$ (Red) configurations of the $q = 2, \chi = 0.7$ system. Bottom panel: the same as above, but for the $q = 4, \chi = 0.8$ system. The legend gives the mass-ratio and spin of signal waveform and the parameter varied between the signal and template waveform. For both systems, $\Delta\beta$ is small during late-inspiral, with the majority of differences arising near merger.

initial data, had been reflected in the orbital plane between the $\phi_{\rm Sn}$ and $\phi_{\rm Sn} + \pi$ configurations.

When we rotate the initial in-plane spin direction $\phi_{\rm Sn}$, this will, by definition, rotate the initial orbital angular momentum about the total angular momentum, i.e., a change in the α Euler angle in Eq. (3). But we do not expect it to have a significant impact on the opening angle β between the orbital and total angular momenta, at least during the inspiral. In Fig. 2 we plot the differences in the β Euler angle for the $q = 2$ and $q = 4$ systems with differences in $\phi_{\rm Sn}$ of $\pi/2$ and π. We can see that $\Delta\beta \sim 0$ for $q = 2$, but rises to a few $\sim\mathcal{O}(1°)$ for $q = 4$; this is consistent with our expectation as the construction of the $q = 2$ series configurations better represent the symmetry. We note that in comparing the $\phi_{\rm Sn} = 0$ and $\phi_{\rm Sn} = \pi/2$ configurations, there is a clear difference in β during the merger and ringdown.

We now wish to estimate how easily two configurations can be distinguished for different choices of binary orientation, (θ, ϕ). In all of these comparisons, we average ρ_c over four choices of waveform polarization. As mentioned in Sec. III A, for each signal system we have $(25 \times 30 \times 4 = 3000)$ match values and the SNR for each. To average across different choices of signal polarisation, ψ^s, we follow Refs. [18,56,57] and average the match for each (θ^s, ϕ^s) across the signal polarization ψ^s by weighting them with their SNR. This approximately accounts for the likelihood of the signal being detected. This SNR-averaged match is defined as,

$$\bar{\mathcal{M}} = \left(\frac{\sum_i \rho_i^3 \mathcal{M}_i^3}{\sum_i \rho_i^3}\right)^{1/3}, \tag{10}$$

where the sum is over all four signal polarization values. So, for a given system, we have 750 values of the SNR averaged match.

Figure 3 shows contour plots of the variation of ρ_c across the signal (θ, ϕ) for the q2a07p90 and q4a08p90 signals as seen by the q2a07p0 and q4a08p0 systems respectively, where the match at each (θ, ϕ) point is maximized over template (θ, ϕ, ψ) and then averaged over the signal ψ values using Eq. (10) and ρ_c is computed using Eq. (9). For these systems with $\phi_{\rm Sn}$ differences of $\pi/2$, the major contribution to the mismatch would be from a combination of their slightly different precession motion (as seen from Fig. 2) and mode-asymmetry behaviour. For the $q = 2$ system, $20 \lesssim \rho_c \lesssim 72$, whereas for the $q = 4$ system, $11 \lesssim \rho_c \lesssim 32$. Precession effects are more pronounced at edge-on than face-on inclination, so the lower ρ_c for q2a07p90 at $\theta \sim \pi/2$ is expected. For q4a08p90, this behaviour seems to reverse (higher ρ_c at edge-on compared to face-on). In Sec. V C, we remove the mode-asymmetry from the waveforms and compute the matches between the symmetrized waveforms for the $\phi_{\rm Sn} = \pi/2$ signals as seen

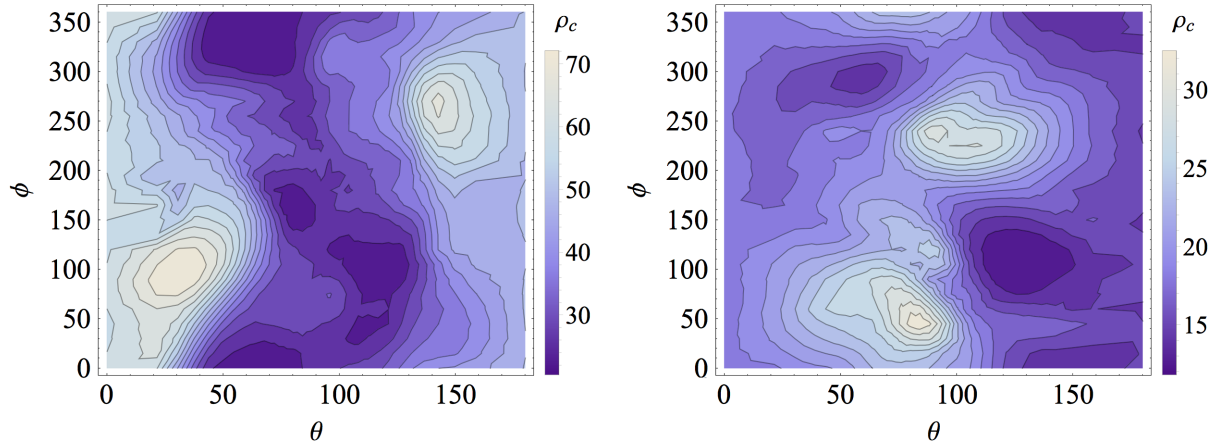

FIG. 3. The left and right panels show the contour plot of ρ_c for the signal q2a07p90 and q4a08p90 as seen by template q2a07p0 and q4a08p0 respectively over the signal (θ, ϕ) values with the label on the right of each plot showing the values of ρ_c. See text for further discussion.

by $\phi_{\rm Sn} = 0$ template. For the $q = 2$ system, the band of low ρ_c near edge-on inclination broadens for all ϕ and for the $q = 4$ system, the peaks of high ρ_c shift slightly away from near edge-on inclinations with an overall increase in ρ_c for both cases. This implies that the behavior of ρ_c across the (θ, ϕ) space can be strongly affected by mode-asymmetric content for these systems.

We see from Fig. 3 that there is a wide variation in the SNR at which these configurations would be distinguishable, depending on their orientation to the detector. Also, the exact way in which precessional motion and mode-asymmetry affect distinguishability over the (θ, ϕ) space is hard to characterize. For the main results in this paper, we find it more instructive to use a measure that would give an idea of the variation of ρ_c across all orientations. For a given signal and template configuration, we define the quantity $\Gamma(\rho)$ which gives the percentage of signals distinguishable at a given SNR by the template. This quantity can be defined formally as,

$$\Gamma(\rho) = 100\frac{\text{len}(\mathcal{S}_{\text{id2:id1}}[\rho_c < \rho])}{\text{len}(\mathcal{S}_{\text{id2:id1}})}, \tag{11}$$

where $\mathcal{S}_{\text{id2:id1}}[\rho_c < \rho]$ is the set of all signals with distinguishability SNR (ρ_c) smaller than a given SNR value (ρ) and $\mathcal{S}_{\text{id2:id1}}$ is the set of all the available signals. In the following sections, this cumulative measure of the fraction of signal distinguishable at a given SNR or lower, will be used as our main tool to quantify the differences between binary configurations.

V. RESULTS

We now consider in detail the distinguishability of our NR configurations. To reiterate, for each system at a given mass-ratio, the $\phi_{\rm Sn} = 0$ system is used as the proxy template waveform. For the results hence, compared to the proxy templates, the signals either have a different spin direction or the magnitude. Also, due to the approximate symmetry between the $\phi_{\rm Sn} \pm \pi$ systems, the results for the $\phi_{\rm Sn} = 3\pi/2$ and $\phi_{\rm Sn} = \pi/2$ are very similar, and hence, we will only present results for the $\phi_{\rm Sn} = \pi/2$ systems.

We first summarise the main differences that we observe between the different configurations, by averaging the match and distinguishability SNR ρ_c over all 3000 orientations and polarizations. The results are shown in Table II. We see that variations in the in-plane spin direction can be distinguishable at an SNR of 60, and sometimes as low as ∼20. Similarly, waveforms from systems with different spin *magnitudes* can be distinguishable are SNRs of ∼60 for spin differences on the order of 0.1. These results encapsulate the two key conclusions we derive from this study: differences in the waveforms between configurations with different in-plane spin directions may be measurable with observations in the near future (the highest BBH SNR to date has been GW150914, with an SNR of ∼24 [58]), and the SNRs at which in-plane spin magnitudes could be measured are comparable to those at which the spin direction will also impact the results. This strongly suggests that waveform changes due to the in-plane spin direction (beyond an overall offset in the precession angle α) need to be included in waveform models.

TABLE I. Table of NR simulations used for this study. From left to right, the columns show the name of the simulation, the mass-ratio of the system, value of the spin on the larger black hole at the reference frequency, the separation between the black holes at the reference frequency, the total momenta of the system at the reference frequency, the reference frequency at which the simulation starts, and the values of the $\phi_{\rm Sn}$ and θ_{SL} angles respectively. For the $q = 1$ series, note that $\mathbf{S}_2 = -\mathbf{S}_1$.

Config	q	$\vec{S}_2$	$\vec{r} = D/M$	$\vec{p} = \vec{p}_1 - \vec{p}_2$	$\omega_{\rm start}(fM)$	$\phi_{\rm Sn}$	θ_{SL}
$\text{q1a08p0}_{\text{sk}}$	1	(0, −0.799, −0.001)	(0, 11.623, 0)	(−0.174, −0.001, 0)	0.0225	0	$\pi/2$
$\text{q1a08p90}_{\text{sk}}$	1	(0.7999, 0, −0.0012)	(0, 11.623, 0)	(−0.174, −0.001, 0)	0.0225	$\pi/2$	$\pi/2$
$\text{q1a08p180}_{\text{sk}}$	1	(0, 0.7999, −0.0012)	(0, 11.623, 0)	(−0.174, −0.001, 0)	0.0225	π	$\pi/2$
$\text{q1a08p270}_{\text{sk}}$	1	(−0.7999, 0, −0.0012)	(0, 11.623, 0)	(−0.174, −0.001, 0)	0.0225	$3\pi/2$	$\pi/2$
q2a07p0	2	(−0.001, 0.699, 0.006)	(0., 10.810, 0.)	(−0.105, −0.001, 0.123)	0.025	0	$\pi/2$
q2a07p90	2	(−0.451, −0.005, 0.535)	(0., 10.810, 0.)	(−0.105, −0.001, 0.123)	0.025	$\pi/2$	$\pi/2$
q2a07p180	2	(0.006, −0.699, −0.002)	(0., 10.810, 0.)	(−0.105, −0.001, 0.123)	0.025	π	$\pi/2$
q2a07p270	2	(0.448, −0.005, −0.537)	(0., 10.810, 0.)	(−0.105, −0.001, 0.123)	0.025	$3\pi/2$	$\pi/2$
q4a08p0	4	(0.0007, 0.799, −0.005)	(0., 11.486, 0.)	(−0.111, −0.0004, 0.014)	0.0225	0	$\pi/2$
q4a08p90	4	(−0.793, 0, 0.099)	(0., 11.486, 0.)	(−0.111, −0.0005, 0.014)	0.0225	$\pi/2$	$\pi/2$
q4a08p180	4	(−0.0007, −0.799, −0.005)	(0., 11.486, 0.)	(−0.111, −0.0004, 0.014)	0.0225	π	$\pi/2$
q4a08p270	4	(0.792, 0, −0.110)	(0., 11.486, 0.)	(−0.111, −0.0005, 0.0147)	0.0225	$3\pi/2$	$\pi/2$
q4a04p0	4	(−0.001, 0.399, −0.00007)	(0., 11.486, 0.)	(−0.111, −0.0004, 0.014)	0.0299	0	$\pi/2$
q2a04p0	2	(−0.00008, 0.3999, −0.0008)	(0., 11.6299, 0.)	(−0.153, −0.0009, 0.015)	0.0224	0	$\pi/2$
q2a08p0	2	(0.0005, 0.799, −0.003)	(0., 11.5709, 0.)	(−0.153, −0.0009, −0.0243)	0.023	0	$\pi/2$

TABLE II. Match and distinguishability SNR ρ_c between different configurations, averaged over all (θ, ϕ, ψ) values. We consider three template waveforms (left), and a variety of different signals. See text for further discussion.

Template	Signal	Average match	ρ_c
$q = 2, \chi = 0.7, \phi_{\rm Sn} = 0$ "q2a07p0"	$\phi_{\rm Sn} + \pi/2$	0.9983	60
	$\phi_{\rm Sn} + \pi$	0.9999	250
	$\chi + 0.1$	0.9983	60
	$\chi - 0.3$	0.9952	36
$q = 4, \chi = 0.8, \phi_{\rm Sn} = 0$ "q4a08p0"	$\phi_{\rm Sn} + \pi/2$	0.9811	17
	$\phi_{\rm Sn} + \pi$	0.9997	143
	$\chi - 0.4$	0.9936	30
$q = 1, \chi = 0.8, \phi_{\rm Sn} = 0$ "q1a08p0$_{\rm sk}$"	$\phi_{\rm Sn} + \pi/2$	0.9981	57
	$\phi_{\rm Sn} + \pi$	0.9998	197

The remainder of this paper considers these results in more detail, and we also attempt to isolate the physical effects that lead to these waveform differences.

In Sec V A we compare the full NR waveforms (using all the $\ell = 2$ multipoles). This allows us to identify the range of SNRs in which the configurations with different choices of $\phi_{\rm Sn}$ will be distinguishable, and to compare this with the effect of changing the in-plane spin magnitude.

We then attempt to isolate the causes of these differences. In Sec. V B, we transform the waveforms into the coprecessing frame (where modes with $|m| < 2 \approx 0$) and study the matches between the waveform with symmetrized $(l, |m|) = (2, 2)$ modes for $\phi_{\rm Sn} \pm \pi/2$ systems. This allows us to estimate the distinguishability of two waveforms when both precession and mode-asymmetry effects are muted, due primarily to small differences in the inspiral rate and merger-ringdown differences. These coprecessing-frame symmetrized modes are then transformed back to the inertial frame and Sec. V C presents the results of analysis with those waveforms. These results estimate the impact of neglecting mode-asymmetry on the distinguishability of precessing-binary waveforms.

A. Full waveform analysis

The key results of this work are shown in Fig. 4. The figure shows the percentage of signals with different spin direction (top panel) or magnitude (bottom panel) that will be distinguishable below a given SNR with the corresponding $\phi_{\rm Sn} = 0$ template for the $q = 1$, 2, 4 systems. In the legend, we mention the mass-ratio and spin of the signal waveform and the parameter varied between the signal and template waveform. Unless mentioned otherwise, for all plots hence, systems with $q = 1$, 2, 4 are color coded with red, black, and blue respectively.

For the $q = 1$ super-kick configurations, the detectability between $\phi_{\rm Sn} \pm \pi/2$ systems is due to asymmetric radiation of gravitational modes. The detectable SNRs for these super-kick systems, $45 \lesssim \rho_c \lesssim 80$, are in the possible range of ground based detectors, but will be rare; we expect less than one in every hundred signals to have such high SNRs. The recoil velocities for the $q = 1$ waveforms used here are $\sim$700 km/s ($\phi_{\rm Sn} = 0$) and $\sim$2700 km/s ($\phi_{\rm Sn} = \pi/2$). For systems with lower spins (and hence lower recoil velocities), we can expect larger values of ρ_c, meaning that these differences will be more difficult to measure. These results are consistent with those presented in Refs. [59,60].

The ρ_c for the $q = 2$ systems with $\phi_{\rm Sn} = \pi/2$ are in the range of $20 \lesssim \rho_c \lesssim 75$, and for $q = 4$ they are $12 \lesssim \rho_c < 35$. Given that GW signals have already been observed with SNRs as high as 30 [61], and the detection threshold is at an

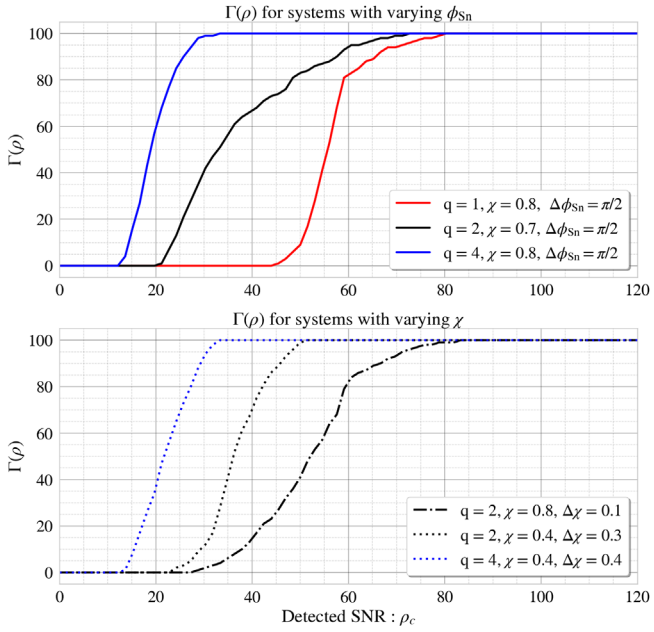

FIG. 4. $\Gamma(\rho)$ as defined in Eq. (11). Top panel: $q = 1$, 2, 4 systems with $\phi_{\rm Sn}$ differences of $\pi/2$. Lower panel: $q = 2$, 4 systems with different spin values. The results for $q = 1$, $q = 2$ and $q = 4$ are shown in red, black, and blue respectively. The solid lines show the results for systems with $\phi_{\rm Sn}$ differences of $\pi/2$ and the same χ_p, the dashed-lines show the results for large χ_p differences (0.3 for $q = 2$ and 0.4 for $q = 4$) with the same $\phi_{\rm Sn}$, and the dotted-dashed for small χ_p differences (0.1 for $q = 2$) with the same $\phi_{\rm Sn}$. See text for further details.

SNR of approximately 10, these are well within the range of current ground-based detectors. We emphasize that these results do not mean we can necessarily measure, for example, the spin direction at the frequency when the signal enters the detector's sensitivity band; this quantity may be degenerate with other physical properties. However, they do indicate that systems with different values of $\phi_{\rm Sn}$ can be distinguished from each other, and if we do not take into account the effects on the waveform of varying $\phi_{\rm Sn}$ (as in current Phenom and EOB models), then these differences will manifest themselves in biases in at least one physical parameter for sufficiently strong signals.

We might expect that the effect of $\phi_{\rm Sn}$ on measurements will be far smaller than that of the spin magnitude. The lower panel of Fig. 4 shows that this is not necessarily the case. For example, the $q = 2$ system with χ_p of 0.8, the distinguishability SNRs are in the range $30 \lesssim \rho_c \lesssim 80$. A change in the spin of 0.1 is therefore, in general, slightly more difficult to distinguish than a change in the in-plane spin direction of $\pi/2$. A change in the spin magnitude of 0.3 (for the $q = 2$, $\chi_p = 0.4$ system) is distinguishable at SNRs in the range $25 \lesssim \rho_c \lesssim 45$. As we can see by comparing with the upper panel, this is comparable to the distinguishability of a spin rotation of $\pi/2$. In the $q = 4$ configurations, we see that a spin change of 0.4 (between 0.8 and 0.4) is distinguishable in the SNR range $13 \lesssim \rho_c < 35$, again comparable to what we see for a spin rotation. These results suggest that the SNRs at which in-plane spin magnitudes become measurable are also the SNRs at which changes in the waveform due to spin rotations also become measurable. As noted above, this study cannot tell us which physical measurements will be biassed by models that neglect mode asymmetries or changes in the binary dynamics, but our results raise the possibility that accurate measurements of precessing systems, i.e., of black-hole spins, will not be possible without the inclusion of some or all of these effects in waveform models.

For the $q = 2$ and $q = 4$ systems with different spin directions, we observe a slight difference in the merger times, mode-asymmetric content as well as precessional dynamics (as can be seen from the $\Delta\beta$ plot in Fig. 2). These differences are the main reason for distinguishability of systems with different spin directions. These effects will become weaker for lower spins, but one should bear in mind that precession effects and black-hole spins will also become more difficult to measure [62]. As such, we expect these results to be largely independent of spin magnitude. A more important caveat on these results is that they are restricted to signals of total mass of 100 $M_\odot$. For lower-mass systems we expect the mode asymmetries to contribute less to the SNR, and therefore to have less impact. We leave a study of the impact of mode asymmetries on parameter measurements to future work.

B. QA frame symmetrized waveform analysis

As mentioned previously, for the $q = 2$ and $q = 4$ systems with different $\phi_{\rm Sn}$, the mismatches are primarily due to differences in their precessional motion (i.e., differences in the $(\alpha, \beta, \epsilon)$ angles) and mode-asymmetric content. In this section our aim is to remove, as much as possible, the precession and mode-asymmetry effects, and to quantify the impact of all other effects (inspiral rate and merger-ringdown behavior). We transform the $q = 2$ and $q = 4$ waveforms into the coprecessing frame (specifically, the quadrupole-aligned, "QA," frame [31–33]) using Eq. (3). This minimizes modulations due to precession. In this frame the dominant power is in the $(\ell = 2, |m| = 2)$ harmonics. We then symmetrize these harmonics, to remove the effects of mode asymmetries. In terms of the QA frame modes (h^{QA}_{lm}), the symmetric waveform in the QA frame $(h^{QA,symm}_{22})$ is defined as,

$$h^{QA,symm}_{22} = \frac{1}{2}(h^{QA}_{22} + h^{*QA}_{2,-2}), \tag{12}$$

where $h^*_{l,m}$ is the complex conjugate of the mode. Using this, we can define the $(2,-2)$ mode as, $h^{QA,symm}_{2,-2} = h^{*QA,symm}_{2,2}$, using the relation $h_{\ell m} = (-1)^\ell h^*_{\ell,-m}$. Doing this for the $q = 2$ and $q = 4$ systems removes the precession modulations and mode-asymmetry. As the super-kick simulations are non-precessing, those waveforms are symmetrized in the inertial frame using Eq. (12).

Matches calculated between symmetrised QA (2,2) modes are independent of orientation and polarization, so the averaging that we performed previously is no longer necessary. Between the $\phi_{\rm Sn} \pm \pi/2$ configurations at mass ratios $q = 1$, 2, 4, the indistinguishability SNRs are now 120, 90 and 30, respectively. If we contrast these with the top panel of Fig. 4, we see that for the $q = 2$ and $q = 4$ cases, differences in the signal phase make a noticeable contribution to the indistinguishability SNR. In Fig. 5 we show ρ_c over a range of $f_{\rm max}$ values. Figure 6 shows the $q = 2$ series waveforms in time and frequency domain, to illustrate where these choices of $f_{\rm max}$ occur during the binaries' coalescence. These figures show that, as we might expect, most of the disagreement between the waveforms accumulates during merger and ringdown.

These results should be taken with a few caveats. As already mentioned, for the $q = 2$ waveforms obtained with 80- and 96-point resolutions, over the θ space, the match lies between 0.9995–0.99995 which translates to ρ_c of ~110–345. So, although the QA frame symmetrized matches are close to the minimum match due to NR uncertainties, over the majority of the θ space, the QA frame symmetrized results should hold even for more accurate NR waveforms. For the $q = 4$ system, to obtain the low eccentricity parameters, the momenta between the

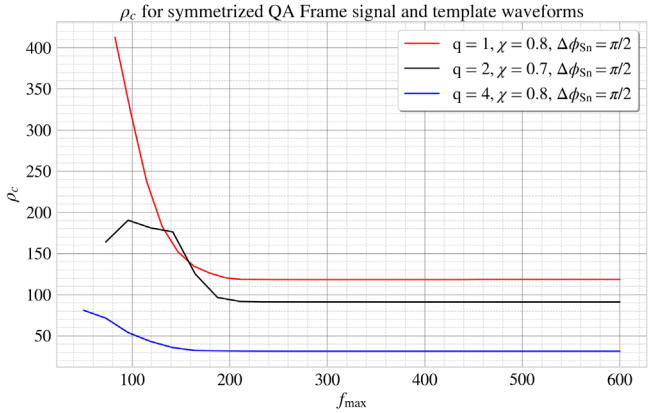

FIG. 5. This plot shows the ρ_c computed from the match ($\mathcal{M}$) between the symmetrized QA frame waveforms for the $q = 2$, $q = 4$ systems (solid-black, solid-blue respectively) and symmetrized $q = 1$ waveforms (solid-red), with varying values of the upper cutoff frequency in $f_{\rm max}$ for the match calculation. The legend follows the same naming convention as Fig: 4.

$\phi_{\rm Sn} = 0, \pi/2$ systems are slightly different, which could be one of the sources of disagreement between the QA-frame symmetrized waveforms. However, the similarity of the trends of the match vs $f_{\rm max}$ for all three systems indicate that the above results should hold within these uncertainties.

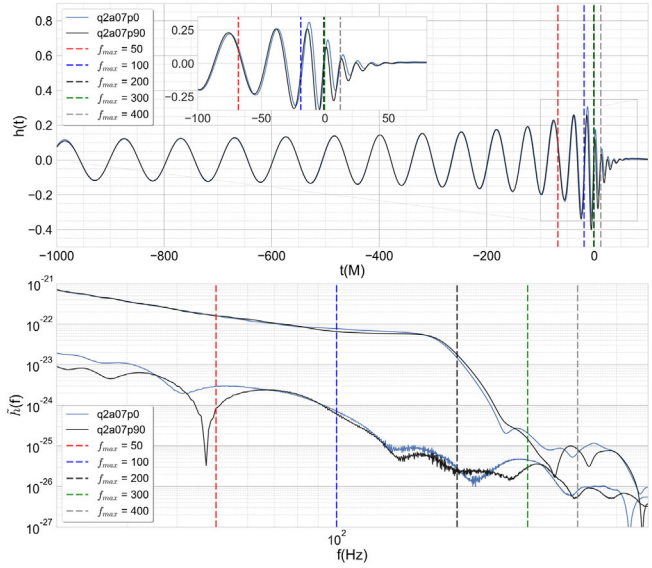

FIG. 6. In the top [bottom] panel, we plot the q2a07p0 (blue) and q2a07p90 (black) time [frequency] domain QA frame symmetrized waveforms. For the top panel, the dashed lines show the time at which the waveform has a specific frequency used as $f_{\rm max}$ value for Fig: 5. For the bottom panel, the dashed lines show the position of that frequency with respect to the frequency domain waveform. Frequency values of (50, 100, 200, 300, 400) are given in dashed (red, blue, black, green, gray) lines respectively.

C. Inertial frame symmetrized waveform analysis

We now transform the symmetrized QA frame waveforms to the inertial frame using Eq. (3) and the corresponding $(\alpha, \beta, \epsilon)$ angles for each system. This is similar to how current waveform models construct the precessing waveforms in the inertial frame, i.e., they transform a model for the corresponding aligned-spin QA frame waveform to the inertial frame using a model for the precession Euler angles. Using these waveforms, we perform the same analysis as in Sec. V A and plot the $\Gamma(\rho)$ quantity in Fig. 7. Note, that for the $q = 1$ system, the symmetrized waveform matches will be the same as presented in Fig. 5 and we will not discuss that system here.

We consider first the two $\phi_{\rm Sn} = \pi/2$ configurations for the $q = 2$ and $q = 4$ systems. Between the symmetrized q2a07 systems, the distinguishability SNR is $25 \lesssim \rho_c \lesssim 115$. Between the symmetrized q4a08 systems, the distinguishability SNR is $25 \lesssim \rho_c \lesssim 60$. In both cases, this is significantly higher than for the waveforms with mode-asymmetry included, and the range is either side of the value for the symmetrized QA-frame waveforms. In particular, we see that the presence of asymmetries makes the q2a07 cases distinguishable at SNRs as low as 20, and the q4a08 cases distinguishable at SNRs as low as 10, while, if the asymmetries did not exist, they would not be distinguishable for SNRs lower than ∼30.

If we now consider the distinguishability between configurations with different spin magnitudes, comparing Figs. 4 and 7, we see a similar effect. Although for $q = 2$ configurations the ρ_c for different spin magnitudes show an overall increase, a few of the signals with a χ_p difference of 0.1 are now easier to distinguish than a χ_p difference of 0.3. The most pronounced effect is for $q = 4$ configurations,

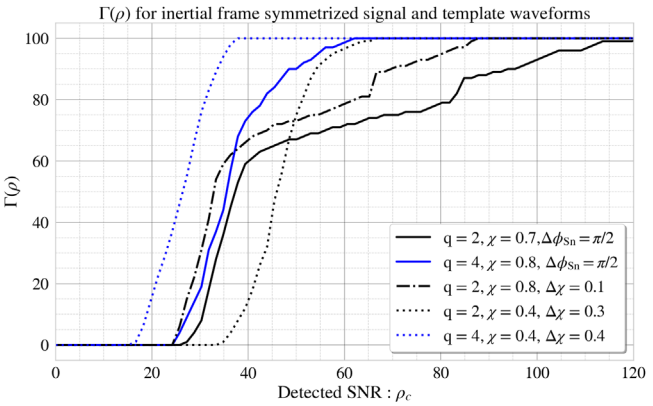

FIG. 7. $\Gamma(\rho)$ from matching waveforms symmetrized in the QA-frame and then transformed back to the inertial frame. The systems q2a07p90 (solid-black), q2a08p0 (dashed-dotted -black), q2a04p0 (dashed-black) are matched with the q2a07p0 proxy template. The q4a08p90 (solid-blue) and q4a04p0 (dashed-blue) systems are matched with q4a08p0 template. The legend shows the mass-ratio and spin of signal and the difference in the relevant parameter with respect to the template.

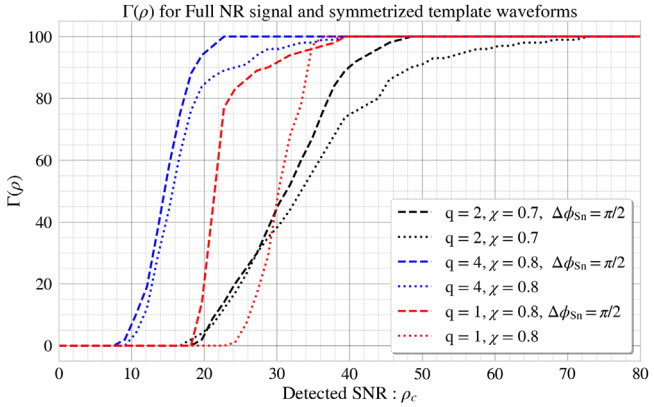

FIG. 8. $\Gamma(\rho)$ from matching signal waveforms with both precession and mode-asymmetry against symmetrized template waveforms. Here, the full waveform $\phi_{\rm Sn} = \pi/2$ signal and $\phi_{\rm Sn} = 0$ signal as seen by the symmetrized $\phi_{\rm Sn} = 0$ template are shown by the dashed and dotted lines respectively. The legend shows the mass-ratio and spin of signal and the difference in the relevant parameter with respect to the template. Where no parameter difference is mentioned, it shows the result for the signal with both precession and mode-asymmetry against its symmetrized self.

where the spin difference of 0.4 is now easier to distinguish than the rotation of the spin.

Neither of the previous analyses reflects the scenario of current GW measurements, where the signals correspond to "full" waveforms, i.e., signals with both precession and mode-asymmetry, and they are analysed using models that correspond approximately to the symmetrized waveforms of the previous analysis. In order to estimate the impact of using symmetrized models in analysis, Fig. 8 shows $\Gamma(\rho)$ for the $\phi_{\rm Sn} = 0, \pi/2$ full waveform signals matched against the symmetrized inertial frame $\phi_{\rm Sn} = 0$ templates for the $q = 1$, $q = 2$ and $q = 4$ simulations. We observe that for $\phi_{\rm Sn} = \pi/2$, it is generally easier for the symmetrized template to distinguish the signal as compared to the full waveform templates. This effect is very strong for the $q = 1$ super-kick cases where the distinguishability SNR reduces by almost 20 for all signals. We also see that removing the mode-asymmetric content leads to large mismatches between waveforms of the same systems causing the full $\phi_{\rm Sn} = 0$ signal to be distinguishable from the symmetrized $\phi_{\rm Sn} = 0$ template at moderate $(10 < \rho_c < 40)$ SNRs for all mass ratios. All these results indicate that the absence of mode asymmetries in current models will lead to measurement biases in these systems. We expect that even for comparable-mass systems, if the total mass is high ($>100\ M_\odot$) and the in-plane spins are high, systematic errors are likely to be significant.

In Table III, we list the SNR averaged match values over all the signal (θ, ϕ, ψ) values to provide one single number for the distinguishability of the signal. We can see that when both signal and templates are symmetrized, for all systems, the agreement between the waveforms increases leading to larger distinguishability SNR. When symmetrized waveform templates are matched with full waveform signals, we see an overall decrease in the distinguishability SNR. Even when both the signal and template systems are the same, with symmetrized templates, ρ_c is comparable to that of $\phi_{\rm Sn} \pm \pi/2$ results.

TABLE III. The SNR averaged match, Eq. (10), over all the (θ, ϕ, ψ) values for the systems considered in this study. From left to right, the columns state the template waveform configuration, difference in the relevant parameter between the template and signal waveform, signal effects (full waveform or symmetrized), teamplate effects (full waveform or symmetrized), average match value and corresponding SNR respectively, using Eq. (9). See text for further discussion.

Template	Signal	Signal effects	Template effects	Average match	ρ_c
	$\phi_{\rm Sn} + \pi/2$	Full	Full	0.9983	60
$q = 2, \chi = 0.7, \phi_{\rm Sn} = 0$ "q2a07p0"	$\phi_{\rm Sn} + \pi/2$	Symmetrized	Symmetrized	0.9991	83
	$\phi_{\rm Sn} + \pi/2$	Full	Symmetrized	0.9954	36
	$\phi_{\rm Sn} + 0$	Full	Symmetrized	0.9969	44
	$\chi + 0.1$	Full	Full	0.9983	60
	$\chi + 0.1$	Symmetrized	Symmetrized	0.9986	65
	$\chi - 0.3$	Full	Full	0.9952	36
	$\chi - 0.3$	Symmetrized	Symmetrized	0.9969	44
$q = 4, \chi = 0.8, \phi_{\rm Sn} = 0$ "q4a08p0"	$\phi_{\rm Sn} + \pi/2$	Full	Full	0.9811	18
	$\phi_{\rm Sn} + \pi/2$	Symmetrized	Symmetrized	0.9935	30
	$\phi_{\rm Sn} + \pi/2$	Full	Symmetrized	0.9737	15
	$\phi_{\rm Sn} + 0$	Full	Symmetrized	0.9785	16
	$\chi - 0.4$	Full	Full	0.9936	30
	$\chi - 0.4$	Symmetrized	Symmetrized	0.9942	32
$q = 1, \chi = 0.8, \phi_{\rm Sn} = 0$ "q1a08p0$_{\rm sk}$"	$\phi_{\rm Sn} + \pi/2$	Full	Full	0.9981	57
	$\phi_{\rm Sn} + \pi/2$	Full	Symmetrized	0.9882	22
	$\phi_{\rm Sn} + 0$	Full	Symmetrized	0.9934	30

VI. CONCLUSIONS

We have investigated when changes in the in-plane spin direction of binary-black-hole systems, the effects of which are not included in current Phenom and EOB models, will be distinguishable in GW measurements. To do that, we use a set of NR simulations obtained from the BAM code (see Table I). We quantify the distinguishability of systems with different choices of in-plane spin direction $\phi_{\rm Sn}$ by calculating matches between them. This approach allows us to estimate the SNR at which the signals will be distinguishable. Our study is restricted to a small number of configurations at mass ratios $q = 1$, 2, 4, and large in-plane spin magnitudes of 0.7 and 0.8, with two configurations with moderate in-plane spin of 0.4. All of our calculations are performed on systems with total mass 100 $M_\odot$.

Changes in $\phi_{\rm Sn}$ have several effects on the binary dynamics and the waveform. One effect that we discuss in detail is the asymmetry between the $\pm m$ waveform modes. Another is small changes in the phasing of the binary, and in the merger and ringdown signal. By removing asymmetry and/or precession effects from our waveforms, we show that all of these effects contribute to the waveform variations between different choices of $\phi_{\rm Sn}$. When mode-asymmetries are muted, the distinguishability SNR ρ_c for *all* the systems (different $\phi_{\rm Sn}$ and different χ_p) show a marked increase across the (θ, ϕ) space (see Fig. 7). Disregarding mode asymmetries increases ρ_c by factors of $\sim$1.5–1.9 between systems of different $\phi_{\rm Sn}$, indicating that this is a significant feature of these waveforms.

Our main results are shown in Sec. V A, and show that for large in-plane spins, variations in $\phi_{\rm Sn}$ will be distinguishable at moderate SNRs. More importantly, these effects will influence measurements at SNRs comparable to those at which in-plane spin magnitudes become measurable. For example, in the $q = 2$ systems we considered, a change in spin magnitude of 0.3 will be distinguishable at a comparable SNR to a change in spin direction of $\pi/2$. This effect will be reduced for smaller spins, but so will our ability to measure the spin magnitude. Precession effects and in-plane spin magnitude, typically captured by the parameter χ_p, have not yet been identified in individual observations [62]. Our results suggest that when they are, the absence of in-plane spin direction effects in the modelling could lead to significant parameter biases. We plan to study the impact on parameter estimation in future work.

There are a number of questions that require further work. We have limited ourselves to small number of configurations, and to one choice of total mass. We have also neglected the effect of $\ell > 2$ modes, which also impact parameter estimation for systems with mass ratios of $q \geq 2$ [63]. The impact of changes in $\phi_{\rm Sn}$, and the importance of mode asymmetries, also needs to be studied for systems with lower masses, where the inspiral contributes more power to the waveform, with mode-asymmetric effects being weaker but with a larger number of precessional cycles. However, in order to fully understand the importance of these physical effects, we require models that include them, which can then be used in parameter-estimation studies. This work has provided strong evidence that these effects must be taken into account in order to make unbiased physical measurements from GW observations, and therefore already provide a strong motivation for such modeling. This has already been done for the surrogate models described in Refs. [64,65]. Since these models are valid only for high-mass systems and a limited range of mass ratios, it would be advantageous to be extended to other classes of model.

ACKNOWLEDGMENTS

We thank Frank Ohme and Sebastian Khan for useful discussions. We thank Edward Fauchon-Jones, Eleanor Hamilton, Charlie Hoy and Dave Yeeles for their help in performing the comparison cases NR simulations. This work was supported by Science and Technology Facilities Council (STFC) Grant No. ST/L000962/1, European Research Council Consolidator Grant No. 647839. We are grateful for computational resources provided by Cardiff University, and funded by an STFC grant supporting UK Involvement in the Operation of Advanced LIGO. Numerical simulations were performed on the DiRAC@Durham facility managed by the Institute for Computational Cosmology on behalf of the STFC DiRAC HPC Facility (www.dirac.ac.uk). The equipment was funded by BEIS capital funding via STFC capital Grants No. ST/P002293/1, No. ST/R002371/1, and No. ST/S002502/1, Durham University and STFC operations Grant No. ST/R000832/1. DiRAC is part of the National e-Infrastructure.

APPENDIX: INITIAL DATA GENERATION

For this study, we required singe-spin precessing NR waveforms with user specified $(\theta_{SL}, \phi_{\rm Sn})$ at a given reference frequency $M\omega_{orb}$. Over the course of inspiral, the spin vectors of a precessing system oscillate about a mean value with the oscillation frequency increasing as system nears merger [48]. An iterative method was required to ensure the required spin direction at the given reference frequency. The code used for solving the PN equations was one which was used for BAM NR waveforms as used in [31,44,46]. The method developed for initial data generation is as below. The PN evolution is started in the $\vec{J}$ aligned to $\hat{z}$ frame with $\vec{L}$ being the Newtonian angular momentum.

The angle between the spin vector and angular momentum vector, (θ_{SL}), varies not more than $\sim 1°$ over the inspiral phase. Hence, once (θ_{SL}) is specified, further iteration is not required To obtain the required $\phi_{\rm Sn}$, the algorithm goes through the following steps:

Step 1:

This step consists of two iterations.

Iteration 1: Initially, both the BHs are placed along the x-axis with a given separation, the orbital plane is the x-y plane, and the initial spin ($\mathbf{S}_{ini}$) parallel to $\hat{n}$. The spin vector is then rotated to obtain the required θ_{SL} and the PN evolution code is run until $M\omega_{orb}$ is reached. We record the time when the specified orbital frequency is reached (t_0), the value of $\phi_{\rm Sn}(t)$ at t_0 [$\phi_{\rm Sn}(t_0)$], the closest time to t_0 at which $\phi_{\rm Sn}(t) = \phi_{\rm Sn}^{\rm target}$, which is denoted t_1, and finally the relative frequency error (ω_{err}) between the orbital frequencies at t_0 and t_1. If, at this iteration, $\phi_{\rm Sn}$ at t_0 is not $\phi_{\rm Sn}^{\rm target}$ or if ω_{err} is larger than a prespecified threshold (ω_{err}^F), the value of $\phi_{\rm Sn}^{t_1}$ is recorded; we call this $\phi_{\rm Sn}^1$. Each iteration hence also stores the value $\phi_{\rm Sn}^{t_0,i}$. For these simulations, we use $\omega_{err}^F = 1\%$.

Iteration 2: During iteration 2, $\mathbf{S}_{ini}$ is rotated to obtain the required θ_{SL} and then further rotated by $(-\phi_{\rm Sn}^1)$ about the z-axis, and then the PN solver is again run. If the conditions specified in Iteration 1 are met ($\omega_{err} < \omega_{err}^F$ & $\phi_{\rm Sn}^{t_1} = \phi_{\rm Sn}^{\rm target}$) then the parameters at t_1 are recorded. If not, we would ideally simply repeat the process. However, since $\phi_{\rm Sn}$ changes on the (rapid) orbital timescale, the value of $\phi_{\rm Sn}$ at the NR reference frequency is very sensitive to the choice at the beginning of the PN evolution, and so this procedure is not well-conditioned to fine-tune $\phi_{\rm Sn}$. We instead proceed to Step Two, and store the value of $\phi_{\rm Sn}^{t_1}$ of this iteration as $\phi_{\rm Sn}^2$.

Step 2: Depending on the parameters, this step can consist of one or multiple iterations. For each iteration, $\mathbf{S}_{ini}$ is rotated to obtain the required θ_{SL} and then by the specified $-\phi_{rot}$ about $\hat{z}$.

Iteration 3: For each iteration hence, we define a angle correction parameter, ϕ_{corr}. $\omega_{err} - \omega_{err}^F$ gives an idea of how close we are to the required initial parameters and value of ϕ_{corr} is based on that. If, $\omega_{err} - \omega_{err}^F > \frac{1}{2}\omega_{err}^F$, then $\phi_{corr} = 10°$, else $\phi_{corr} = 5°$ and then $\phi_{rot} = \phi_{\rm Sn}^2 + \phi_{corr}$. Using these angles, the spin is rotated and PN solver is run. Again, the value of $\phi_{\rm Sn}^{t_1}$ of this iteration as $\phi_{\rm Sn}^3$.

Iteration $n > 3$: First, we check if $\phi_{\rm Sn}^3 > \phi_{\rm Sn}^2$. If so, the initial spin is being rotated in the wrong direction and for each subsequent iteration, $\phi_{rot} = \phi_{\rm Sn}^2 - (n-3)\times \phi_{corr}$, if not, $\phi_{rot} = \phi_{\rm Sn}^2 + (n-2)\times\phi_{corr}$. Thus, we brute force the initial direction of $\mathbf{S}_{ini}$ until the required direction of $\mathbf{S}$ is obtained at the reference frequency.

To apply this procedure with a higher tolerance, one should reduce ϕ_{corr} in subsequent iterations. For the simulations produced here, no more than two or three iterations in step two were required.

[1] J. Aasi *et al.*, Advanced LIGO, Classical Quantum Gravity **32**, 115012 (2015).

[2] F. Acernese *et al.*, Advanced Virgo: A second-generation interferometric gravitational wave detector, Classical Quantum Gravity **32**, 024001 (2015).

[3] B. P. Abbott *et al.*, GWTC-1: A gravitational-wave transient catalog of compact binary mergers observed by LIGO and Virgo during the first and second observing runs, 2018.

[4] R. Abbott *et al.*, GWTC-2: Compact binary coalescences observed by LIGO and Virgo during the first half of the third observing run, arXiv:2010.14527.

[5] A. H. Nitz, T. Dent, G. S. Davies, S. Kumar, C. D. Capano, I. Harry, S. Mozzon, L. Nuttall, A. Lundgren, and M. Tápai, 2-OGC: Open gravitational-wave catalog of binary mergers from analysis of public advanced LIGO and virgo data, Astrophys. J. **891**, 123 (2020).

[6] B. Zackay, L. Dai, T. Venumadhav, J. Roulet, and M. Zaldarriaga, Detecting gravitational waves with disparate detector responses: Two new binary black hole mergers, arXiv:1910.09528.

[7] T. Venumadhav, B. Zackay, J. Roulet, L. Dai, and M. Zaldarriaga, New binary black hole mergers in the second observing run of Advanced LIGO and Advanced Virgo, Phys. Rev. D **101**, 083030 (2020).

[8] R. Abbott *et al.*, GW190814: Gravitational waves from the coalescence of a 23 Solar mass black hole with a 2.6 Solar mass compact object, Astrophys. J. **896**, L44 (2020).

[9] R. Abbott *et al.*, GW190412: Observation of a binary-black-hole coalescence with asymmetric masses, Phys. Rev. D **102**, 043015 (2020).

[10] B. Abbott *et al.*, GW190425: Observation of a compact binary coalescence with total mass ~3.4 $M_\odot$, Astrophys. J. Lett. **892**, L3 (2020).

[11] R. Abbott *et al.*, GW190521: A Binary Black Hole Merger with a Total Mass of 150 $M_\odot$, Phys. Rev. Lett. **125**, 101102 (2020).

[12] B. Abbott *et al.*, Binary black hole population properties inferred from the first and second observing runs of Advanced LIGO and Advanced Virgo, Astrophys. J. Lett. **882**, L24 (2019).

[13] R. Abbott *et al.*, Properties and astrophysical implications of the 150 Msun binary black hole merger GW190521, Astrophys. J. Lett. **900**, L13 (2020).

[14] R. Abbott *et al.*, Population properties of compact objects from the second LIGO-Virgo gravitational-wave transient catalog, arXiv:2010.14533.

[15] S. Khan, S. Husa, M. Hannam, F. Ohme, M. Pürrer, X. Jiménez Forteza, and A. Bohé, Frequency-domain gravita-

tional waves from nonprecessing black-hole binaries. II. A phenomenological model for the advanced detector era, Phys. Rev. D **93**, 044007 (2016).
[16] L. London, S. Khan, E. Fauchon-Jones, C. García, M. Hannam, S. Husa, X. Jiménez-Forteza, C. Kalaghatgi, F. Ohme, and F. Pannarale, First Higher-Multipole Model of Gravitational Waves from Spinning and Coalescing Black-Hole Binaries, Phys. Rev. Lett. **120**, 161102 (2018).
[17] M. Hannam, P. Schmidt, A. Bohé, L. Haegel, S. Husa, F. Ohme, G. Pratten, and M. Pürrer, Simple Model of Complete Precessing Black-Hole-Binary Gravitational Waveforms, Phys. Rev. Lett. **113**, 151101 (2014).
[18] S. Khan, K. Chatziioannou, M. Hannam, and F. Ohme, Phenomenological model for the gravitational-wave signal from precessing binary black holes with two-spin effects, Phys. Rev. D **100**, 024059 (2019).
[19] G. Pratten, S. Husa, C. Garcia-Quiros, M. Colleoni, A. Ramos-Buades, H. Estelles, and R. Jaume, Setting the cornerstone for a family of models for gravitational waves from compact binaries: The dominant harmonic for nonprecessing quasicircular black holes, Phys. Rev. D **102**, 064001 (2020).
[20] G. Pratten *et al.*, Let's twist again: Computationally efficient models for the dominant and sub-dominant harmonic modes of precessing binary black holes, arXiv:2004.06503.
[21] A. Bohé *et al.*, Improved effective-one-body model of spinning, nonprecessing binary black holes for the era of gravitational-wave astrophysics with advanced detectors, Phys. Rev. D **95**, 044028 (2017).
[22] R. Cotesta, A. Buonanno, A. Bohé, A. Taracchini, I. Hinder, and S. Ossokine, Enriching the symphony of gravitational waves from binary black holes by tuning higher harmonics, Phys. Rev. D **98**, 084028 (2018).
[23] Y. Pan, A. Buonanno, A. Taracchini, L. E. Kidder, A. H. Mroué, H. P. Pfeiffer, M. A. Scheel, and B. Szilágyi, Inspiral-merger-ringdown waveforms of spinning, precessing black-hole binaries in the effective-one-body formalism, Phys. Rev. D **89**, 084006 (2014).
[24] S. Babak, A. Taracchini, and A. Buonanno, Validating the effective-one-body model of spinning, precessing binary black holes against numerical relativity, Phys. Rev. D **95**, 024010 (2017).
[25] A. Taracchini *et al.*, Effective-one-body model for black-hole binaries with generic mass ratios and spins, Phys. Rev. D **89**, 061502 (2014).
[26] A. Ramos-Buades, P. Schmidt, G. Pratten, and S. Husa, Validity of common modeling approximations for precessing binary black holes with higher-order modes, Phys. Rev. D **101**, 103014 (2020).
[27] F. Herrmann, I. Hinder, D. Shoemaker, P. Laguna, and R. A. Matzner, Gravitational recoil from spinning binary black hole mergers, Astrophys. J. **661**, 430 (2007).
[28] C. García-Quirós, M. Colleoni, S. Husa, H. Estellés, G. Pratten, A. Ramos-Buades, M. Mateu-Lucena, and R. Jaume, Multimode frequency-domain model for the gravitational wave signal from nonprecessing black-hole binaries, Phys. Rev. D **102**, 064002 (2020).
[29] S. Ossokine *et al.*, Multipolar effective-one-body waveforms for precessing binary black holes: Construction and validation, Phys. Rev. D **102**, 044055 (2020).
[30] S. Khan, F. Ohme, K. Chatziioannou, and M. Hannam, Including higher order multipoles in gravitational-wave models for precessing binary black holes, Phys. Rev. D **101**, 024056 (2020).
[31] P. Schmidt, M. Hannam, and S. Husa, Towards models of gravitational waveforms from generic binaries: A simple approximate mapping between precessing and non-precessing inspiral signals, Phys. Rev. D **86**, 104063 (2012).
[32] M. Boyle, R. Owen, and H. P. Pfeiffer, A geometric approach to the precession of compact binaries, Phys. Rev. D **84**, 124011 (2011).
[33] R. O'Shaughnessy, B. Vaishnav, J. Healy, Z. Meeks, and D. Shoemaker, Efficient asymptotic frame selection for binary black hole spacetimes using asymptotic radiation, Phys. Rev. D **84**, 124002 (2011).
[34] L. E. Kidder, Coalescing binary systems of compact objects to $(\text{post})^{5/2}$-newtonian order. v. spin effects, Phys. Rev. D **52**, 821 (1995).
[35] B. Bruegmann, J. A. Gonzalez, M. Hannam, S. Husa, and U. Sperhake, Exploring black hole superkicks, Phys. Rev. D **77**, 124047 (2008).
[36] R. O'Shaughnessy, L. London, J. Healy, and D. Shoemaker, Precession during merger: Strong polarization changes are observationally accessible features of strong-field gravity during binary black hole merger, Phys. Rev. D **87**, 044038 (2013).
[37] L. Pekowsky, R. O'Shaughnessy, J. Healy, and D. Shoemaker, Comparing gravitational waves from nonprecessing and precessing black hole binaries in the corotating frame, Phys. Rev. D **88**, 024040 (2013).
[38] M. Boyle, L. E. Kidder, S. Ossokine, and H. P. Pfeiffer, Gravitational-wave modes from precessing black-hole binaries, arXiv:1409.4431.
[39] M. Campanelli, C. O. Lousto, Y. Zlochower, and D. Merritt, Maximum Gravitational Recoil, Phys. Rev. Lett. **98**, 231102 (2007).
[40] J. A. Gonzalez, M. D. Hannam, U. Sperhake, B. Bruegmann, and S. Husa, Supermassive Recoil Velocities for Binary Black-Hole Mergers with Antialigned Spins, Phys. Rev. Lett. **98**, 231101 (2007).
[41] S. Husa, J. A. González, M. Hannam, B. Brügmann, and U. Sperhake, Reducing phase error in long numerical binary black hole evolutions with sixth-order finite differencing, Classical Quantum Gravity **25**, 105006 (2008).
[42] B. Brügmann, J. A. González, M. Hannam, S. Husa, U. Sperhake, and W. Tichy, Calibration of moving puncture simulations, Phys. Rev. D **77**, 024027 (2008).
[43] E. Fauchon-Jones, C. Kalaghatgi, E. Hamilton, D. Yeeles, C. Hoy, M. Hannam, A. Vano-Vinuales, J. Thompson, L. T. London, and S. Khan, Bam catalogue of binary black hole simulations (to be published).
[44] M. Hannam, S. Husa, F. Ohme, D. Muller, and B. Bruegmann, Simulations of black-hole binaries with unequal masses or nonprecessing spins: Accuracy, physical properties, and comparison with post-Newtonian results, Phys. Rev. D **82**, 124008 (2010).
[45] M. Purrer, S. Husa, and M. Hannam, An Efficient iterative method to reduce eccentricity in numerical-relativity simulations of compact binary inspiral, Phys. Rev. D **85**, 124051 (2012).

[46] S. Husa, S. Khan, M. Hannam, M. Pürrer, F. Ohme, X. Jiménez Forteza, and A. Bohé, Frequency-domain gravitational waves from nonprecessing black-hole binaries. I. New numerical waveforms and anatomy of the signal, Phys. Rev. D **93**, 044006 (2016).
[47] S. Husa, M. Hannam, J. A. González, U. Sperhake, and B. Brügmann, Reducing eccentricity in black-hole binary evolutions with initial parameters from post-newtonian inspiral, Phys. Rev. D **77**, 044037 (2008).
[48] P. Schmidt, F. Ohme, and M. Hannam, Towards models of gravitational waveforms from generic binaries II: Modelling precession effects with a single effective precession parameter, Phys. Rev. D **91**, 024043 (2015).
[49] E. Baird, S. Fairhurst, M. Hannam, and P. Murphy, Degeneracy between mass and spin in black-hole-binary waveforms, Phys. Rev. D **87**, 024035 (2013).
[50] E. E. Flanagan and S. A. Hughes, Measuring gravitational waves from binary black hole coalescences: 2. The waves' information and its extraction, with and without templates, Phys. Rev. D **57**, 4566 (1998).
[51] L. Lindblom, B. J. Owen, and D. A. Brown, Model waveform accuracy standards for gravitational wave data analysis, Phys. Rev. D **78**, 124020 (2008).
[52] S. T. McWilliams, B. J. Kelly, and J. G. Baker, Observing mergers of non-spinning black-hole binaries, Phys. Rev. D **82**, 024014 (2010).
[53] H.-S. Cho, E. Ochsner, R. O'Shaughnessy, C. Kim, and C.-H. Lee, Gravitational waves from black hole-neutron star binaries: Effective Fisher matrices and parameter estimation using higher harmonics, Phys. Rev. D **87**, 024004 (2013).
[54] K. Chatziioannou, A. Klein, N. Yunes, and N. Cornish, Constructing gravitational waves from generic spin-precessing compact binary inspirals, Phys. Rev. D **95**, 104004 (2017).
[55] M. Pürrer and C.-J. Haster, Ready for what lies ahead?—Gravitational waveform accuracy requirements for future ground based detectors, Phys. Rev. Research **2**, 023151 (2020).
[56] I. Harry, J. Calderón Bustillo, and A. Nitz, Searching for the full symphony of black hole binary mergers, Phys. Rev. D **97**, 023004 (2018).
[57] A. Buonanno, Y.-b. Chen, and M. Vallisneri, Detecting gravitational waves from precessing binaries of spinning compact objects: Adiabatic limit, Phys. Rev. D **67**, 104025 (2003); Erratum, Phys. Rev. D **74**, 029904 (2006).
[58] B. Abbott *et al.*, Binary Black Hole Mergers in the First Advanced LIGO Observing Run, Phys. Rev. X **6**, 041015 (2016); Erratum, Phys. Rev. X **8**, 039903 (2018).
[59] V. Varma, M. Isi, and S. Biscoveanu, Extracting the Gravitational Recoil from Black Hole Merger Signals, Phys. Rev. Lett. **124**, 101104 (2020).
[60] C. O. Lousto and J. Healy, Kicking gravitational wave detectors with recoiling black holes, Phys. Rev. D **100**, 104039 (2019).
[61] B. Abbott *et al.*, GW170817: Observation of Gravitational Waves from a Binary Neutron Star Inspiral, Phys. Rev. Lett. **119**, 161101 (2017).
[62] S. Fairhurst, R. Green, M. Hannam, and C. Hoy, When will we observe binary black holes precessing? Phys. Rev. D **102**, 041302(R) (2020).
[63] C. Kalaghatgi, M. Hannam, and V. Raymond, Parameter estimation with a spinning multimode waveform model, Phys. Rev. D **101**, 103004 (2020).
[64] J. Blackman, S. E. Field, M. A. Scheel, C. R. Galley, C. D. Ott, M. Boyle, L. E. Kidder, H. P. Pfeiffer, and B. Szilágyi, Numerical relativity waveform surrogate model for generically precessing binary black hole mergers, Phys. Rev. D **96**, 024058 (2017).
[65] V. Varma, S. E. Field, M. A. Scheel, J. Blackman, D. Gerosa, L. C. Stein, L. E. Kidder, and H. P. Pfeiffer, Surrogate models for precessing binary black hole simulations with unequal masses, Phys. Rev. Research **1**, 033015 (2019).